

Response regimes in on-chip THz spectroscopy

Gunda Kipp,^{1,2,*} Marios H. Michael,^{3,1,2} Alexander M. Potts,^{1,2,4} Dorothee Herrmann,^{1,2} Toru Matsuyama,^{1,2} Guido Meier,^{1,2} Matthew W. Day,^{1,2,4} Hope M. Bretscher,^{1,2,4} and James W. McIver^{1,2,4,†}

¹Max Planck Institute for the Structure and Dynamics of Matter

²Center for Free-Electron Laser Science (CFEL), Luruper Chaussee 149, 22761 Hamburg, Germany

³Max Planck Institute for the Physics of Complex Systems, Nöthnitzer Straße 38, 01187 Dresden, Germany

⁴Department of Physics, Columbia University, 538 West 120th Street, New York, NY 10027, USA

(Dated: December 1, 2025)

On-chip THz spectroscopy enables quantitative measurements of the optical conductivity of sub-wavelength 2D materials by tightly confining THz fields in metallic transmission line structures interfaced to the material. However, because the probed structures are smaller than the THz wavelength, finite-size and environmental effects can strongly influence the measured response. Here, we identify the conditions under which a metallic sample exhibits a genuine Drude response and when finite-size and environmental effects must be considered. We further introduce and characterize an additional regime, the Phantom-Drude response, which mimics Drude behavior but instead originates from the superposition of multiple finite-momentum plasmonic resonances. If unrecognized, this regime can lead to misinterpretation of intrinsic material properties. We systematically show how the Phantom-Drude response can emerge and demonstrate its sensitivity to sample dimensions, transmission line geometry, material shape, and gate properties, providing practical guidelines to avoid this regime in future on-chip THz measurements.

Introduction. Two-dimensional (2D) materials and van der Waals (vdW) heterostructures host a variety of emergent, gate-tunable phenomena^{1–7}. Many of these, such as superconductivity, correlated insulating states, and strange-metal phases, arise at μeV - meV energy scales^{8–13}, corresponding to terahertz (THz) frequencies. While conventional far-field THz techniques can access these frequencies, they are diffraction-limited and cannot resolve micron-scale samples smaller than the THz wavelength. This limitation has spurred the development of near-field THz techniques capable of probing sub-wavelength structures^{14–21}. Crucially, signals from sub-wavelength samples can differ qualitatively from far-field measurements of large-area samples, as finite-size and environmental effects dominate at small scales²².

Of the available near-field methods, on-chip THz spectroscopy^{23–31} is uniquely suited to probe the influence of sub-wavelength THz effects on a sample's response, because there is an analytical mapping between the near-field signal and the intrinsic conductivity³². In this approach, vdW heterostructures are integrated into ultrafast optoelectronic circuits^{33–38} that confine THz fields using lithographically defined metallic transmission lines (Fig. 1a). Femtosecond laser pulses excite photoconductive switches that launch and detect THz signals, enabling time-resolved transmission or reflection measurements. By using an *in situ* calibration arm³⁹ and incorporating circuit geometry into the analysis²³, the real and imaginary parts of the complex near-field conductivity, $\sigma_{\text{near-field}}$, can be extracted, which directly reflects both the intrinsic electronic response and local dielectric environment.

Previous on-chip THz spectroscopy works have interpreted the optical conductivity of metallic samples in

one of two ways. One group of studies attributed the spectral features to a Drude response^{26–28,40}, where zero-momentum charge transport is governed by electron scattering and dissipation. Another set of studies reported finite-momentum plasmonic resonances^{23–25}, arising from standing wave patterns of current density that are reflected off of both the edges of the transmission lines and the edges of the THz sub-wavelength 2D material. Here, the material effectively forms a plasmonic *self-cavity* for THz light³² (see inset of Fig. 1b). The coexistence of these two interpretations in the literature highlights the importance of identifying the conditions under which each applies to ensure the accurate extraction of material parameters.

In this work, we analytically examine the factors that give rise to Drude or cavity responses and identify an intermediate regime, the *Phantom-Drude* response, which, if unrecognized, can lead to erroneous interpretations. While it is known that time-domain reflections or poor choice of window functions can obscure spectral features from collective modes⁴¹, we show that the Phantom-Drude response arises from a fundamentally different mechanism: the superposition of multiple, inhomogeneously broadened finite-momentum plasmonic collective modes. As illustrated in Fig. 1b, the overlap of several distinct plasmon resonances (blue) can produce a broad, featureless spectrum (red). Such a spectrum appears Drude-like when the measurement bandwidth is limited to be in the range of 0.1 THz to 1 THz, as is often the case experimentally. However, fitting such a spectrum with a Drude model (gold dashed line), leads to the extraction of material parameters that can be 10 % to 400 % off from their intrinsic values.

We analyze three mechanisms underlying the

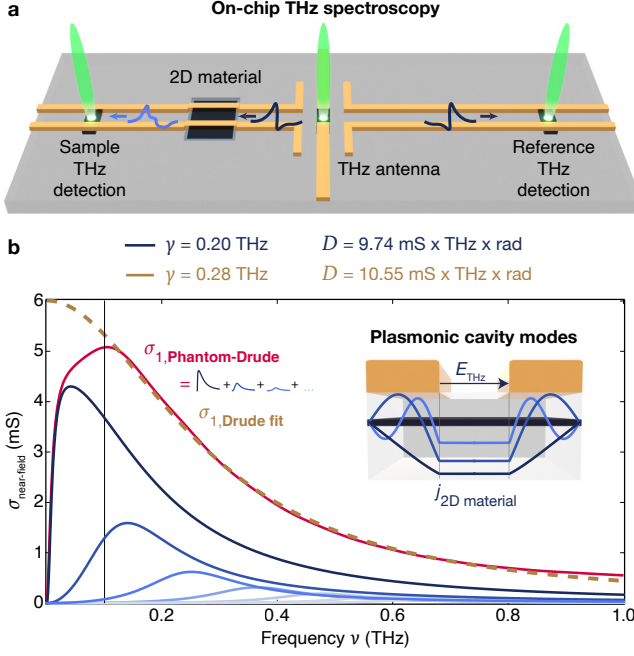


FIG. 1. Probing the near-field optical conductivity of 2D materials with on-chip THz spectroscopy: **a** Schematic of the on-chip THz circuit architecture: Two identical THz pulses (dark blue) propagate along symmetric transmission lines; one interacts with a 2D material (blue gradient) and is detected on the left, while the other serves as a reference on the right. Comparing both signals yields the material's near-field optical conductivity. **b** 2D materials embedded in on-chip THz spectroscopy circuitry form plasmonic self-cavities, featuring one or more resonances in the near-field optical conductivity spectrum²³. These resonances arise from finite-momentum standing waves of current density spanning the sample, as illustrated for the three lowest frequency modes of $\sigma_{\text{near-field}}$ (blue). When the resonance linewidth γ and the frequency resolution are broader than the mode spacing, overlapping resonances merge into a broad spectrum that mimics a Drude response (red), despite being fundamentally different. A Drude fit to the red spectrum (gold dashed curve) yields misleading parameters: the extracted scattering rate γ and Drude weight D (gold) differ significantly from the intrinsic material values (blue). We discuss the origin of this effect and mitigation strategies in this work. Sample parameters for calculations: $W_0 = 0 \mu\text{m}$ (2D material width exceeding the metal strips), $W_1 = 10 \mu\text{m}$ (width of each metal trace) and $W_2 = 10 \mu\text{m}$ (width of the gap between strips), $d_{\text{gold}} = 285 \text{ nm}$ (gold thickness), $d_{\text{hBN}} = 20 \text{ nm}$ (hBN thickness), $d_{\text{sapphire}} = 2 \text{ mm}$ (sapphire substrate thickness), $D = 9.74 \text{ mS} \times \text{THz} \times \text{rad}$ (Drude weight of the 2D material) and $\gamma = 0.2 \text{ THz}$ (scattering rate of the 2D material).

Phantom-Drude regime, arising from the transmission line design, sample geometry, and choice of gate materials, and provide practical design guidelines to mitigate them. These insights enable future on-chip THz spectroscopy studies to reliably probe the intrinsic properties of vdW heterostructures.

Mechanism 1: Reflection of current set by transmission line design. The analytical framework for on-chip THz spectroscopy^{23,32} calculates the effective near-field conductivity for structures where an insulating layer separates the 2D material from the transmission line, capturing how the response is shaped by both the sample geometry and the local dielectric environment. The theory shows that the THz field, largely confined between the transmission line metal strips, drives in-plane currents in the 2D metallic layers perpendicular to the pulse propagation direction (see inset of Fig. 1b). At screened regions beneath the metal traces (W_1), the unscreened gap between the traces (W_2), and the material regions extending beyond the width of the transmission line (W_0), these currents undergo partial reflection and transmission (see Fig. 2a), due to the different dispersion relations of screened and unscreened plasmons.

In the screened regions, the currents form plasmons with low-frequency resonances $\omega_1 = \sqrt{Dq_1^2 d / \epsilon_0 \epsilon_1}$, while in the unscreened regions the resonances shift to higher frequencies $\omega_{0,2} = \sqrt{Dq_{0,2} / \epsilon_0 (\epsilon_1 + \epsilon_2)}$, and $\omega = 2\pi\nu$. Here, D is the Drude weight, defining $\sigma_{\text{Drude}} = D / (2\pi(\gamma - i\nu))$ with scattering rate γ , ϵ_0 is the vacuum permittivity, d and ϵ_1 denote the thickness and dielectric constant of the insulating layer, and ϵ_2 the substrate dielectric. The plasmon momenta are set by the widths of the corresponding regions ($q_{0,1} \approx a\pi / (2W_{0,1})$ and $q_2 \approx a\pi / W_2$, with $a = 1, 3, 5, \dots$). Each permitted momentum, and therefore each excited plasmon wavelength (see inset of Fig. 1b), selects a distinct point on the dispersion relation, giving rise to a corresponding resonance.

Accounting for all boundary conditions (Refs.^{23,32}), the overall effective near-field conductivity of the entire heterostructure is given by:

$$\sigma_{\text{near-field}} = \sigma_{\text{Drude}} (1 + F), \quad (1)$$

with the feedback factor for $W_0 = 0$ (see SI for $W_0 \neq 0$)³²

$$F = \frac{q_2}{-q_2 \cos(q_2 W_2 / 2) + q_1 \sin(q_2 W_2 / 2) \tan(q_1 W_1)}. \quad (2)$$

Here, the finite momenta in the dissipative limit are given by $q_1 = \sqrt{\epsilon_0 \epsilon_1 \omega (\omega + 2\pi i \gamma) / (dD)}$ and $q_2 = \epsilon_0 (\epsilon_1 + \epsilon_2) \omega (\omega + 2\pi i \gamma) / D$. As shown in Equations 1 and 2, the feedback factor F alone determines whether the effective near-field conductivity follows a Drude response ($F \approx 0$) or exhibits self-cavity effects with well-defined plasmonic resonances ($F \neq 0$). Since F depends on the 2D material's Drude weight D , the sample geometry (W_1 , W_2 , d , and W_0), the surrounding dielectric environment (ϵ_1 and ϵ_2), and the scattering rate γ , the type of response observed in on-chip THz spectroscopy is entirely determined by the sample's conductivity, dimensions, and transmission line design.

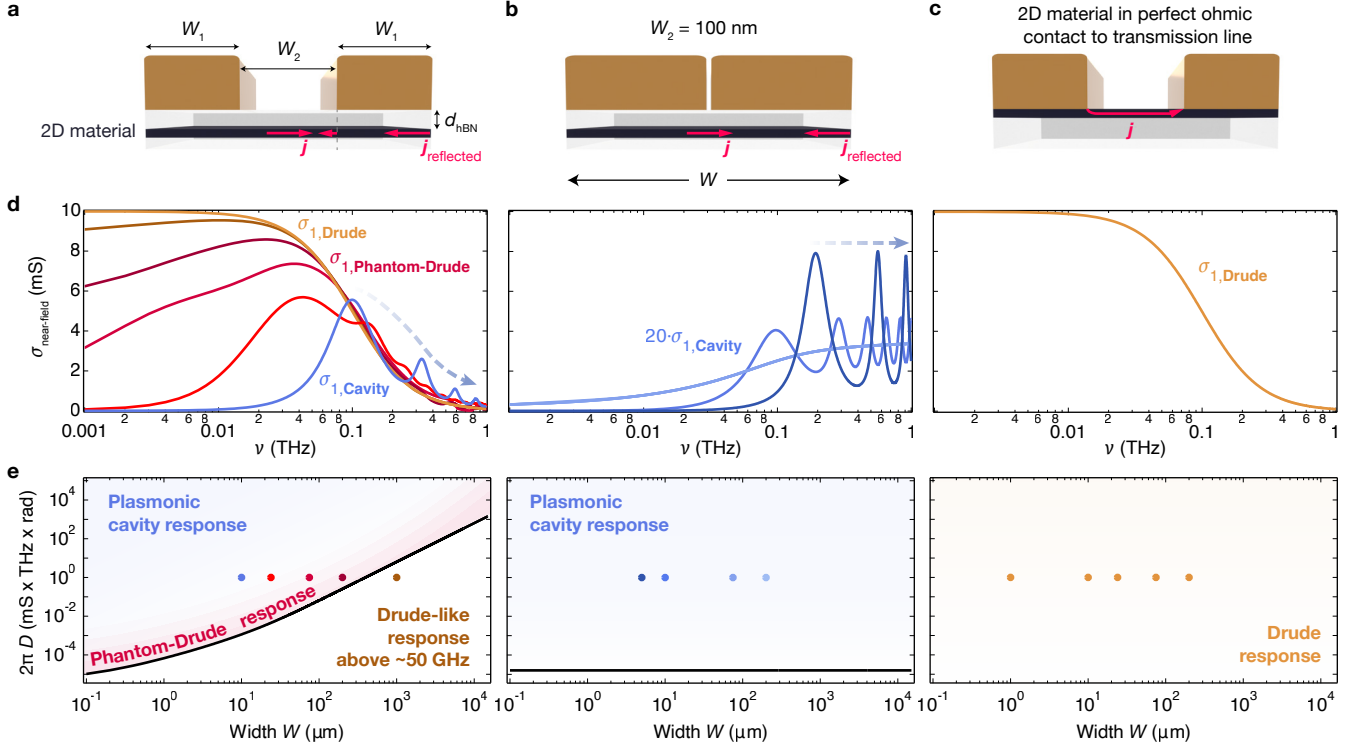


FIG. 2. Impact of transmission line design and material conductivity on the measured response: Three transmission line designs are investigated. **a** In the first design, a 2D material is electrically insulated from the transmission line by a hBN layer of thickness $d_{\text{hBN}} = 20$ nm. The structure is embedded within a transmission line of total width $W = 2W_1 + W_2$ with $W_1 = W_2$. No material is extending beyond the transmission line ($W_0 = 0$, see SI). **b** In the second design, the transmission line has a small gap of width $W_2 = 100$ nm that is kept constant while tuning the overall width W . **c** In the third design, the hBN spacer is removed and the 2D material is placed in perfect ohmic contact to the transmission line of total width $W = 2W_1 + W_2$ with $W_1 = W_2$. **d** displays the real parts of the near-field optical conductivity as function of frequency corresponding to the markers in panels (e). **e** The nature of the response (whether plasmonic cavity, Phantom-Drude, or Drude) is calculated as a function of W and the intrinsic Drude weight D of the material, assuming a fixed scattering rate of 0.1 THz, for each of the three designs illustrated in (a)–(c). For the design shown in (a), any of the three responses (plasmonic cavity, phantom-Drude, or Drude) can be observed depending on W and D . In contrast, the design in (b) permits only cavity responses or broad spectral features that do not resemble a Drude response. The design in (c), featuring an ohmic contact, consistently produces a Drude response regardless of W or D . The black curves in the left (data adapted from Fig. 2d of Ref.²³) and center panel mark parameter sets (D , W) for which the real part of the near-field optical conductivity, measured via on-chip THz spectroscopy, deviates less than 10 % from the intrinsic 2D conductivity at 10 GHz. Notably, the phantom-Drude regime (red-shaded area in (e)) expands with increasing linewidth, while the black curve remains fixed. Note that for design (c), full 3D electromagnetic simulations were used in place of the analytical theory (see SI).

We therefore theoretically examine three distinct transmission line designs to highlight how they govern the near-field response (see Fig. 2): (a) a transmission line with equal metal trace and gap widths ($W_1 = W_2$), where an insulating hBN layer electrically isolates the 2D material from the transmission line, (b) a design with a small gap width ($W_2 \ll W_1$), also incorporating an hBN spacer, and (c) a configuration identical to (a) but without an hBN layer, allowing the 2D material to form an ohmic contact with the transmission line. We then calculated the near-field optical conductivity for a metallic sample with Drude weight $D = 6.28 \text{ mS} \times \text{THz} \times \text{rad}$ and scattering rate $\gamma = 0.1$ THz. These values are representative of a thin graphite or gated graphene flake, providing an illustrative example of materials that display a Drude

response in the far-field but exhibit plasmonic behavior in the near-field^{23,42}. We evaluated the response over a range of sample widths W (see Fig. 2d) and mapped the resulting response types as a function of both D and the total sample width W for each transmission line geometry (see Fig. 2e). The black contours in Fig. 2e indicate the boundary within which the near-field optical conductivity deviates by less than 10 % from the intrinsic Drude conductivity at 10 GHz, corresponding to $|F| < 0.1$ at 10 GHz and $F \approx 0$ at frequencies within the typical experimental bandwidth (see Fig. S18 of Ref.²³). We chose this benchmark because a Drude response is recovered above 10 GHz and scattering rates and Drude weights can be accurately extracted.

For design (a), plasmonic resonances appear promi-

nently in the near-field optical conductivity of a sample with Drude weight $D = 6.28 \text{ mS} \times \text{THz} \times \text{rad}$ and a narrow total width $W = 2W_1 + W_2 = 10 \mu\text{m}$ (blue trace, Fig. 2d). As W increases, the resonances shift to lower frequencies (red traces), and their superposition produces a Phantom-Drude response that persists up to $W = 200 \mu\text{m}$ for this Drude weight. Only for widths approaching $W \sim 1 \text{ mm}$ (dark golden trace) does the spectrum begin to resemble a Drude response above $\sim 50 \text{ GHz}$. Because current on-chip THz circuits typically lack reliable sensitivity below approximately 50 GHz to 100 GHz due to time-domain reflections, such a spectrum could be fit with a Drude model to reliably extract intrinsic material parameters.

However, widths approaching 1 mm remain challenging to realize for vdW heterostructures. A Drude-like response at experimentally accessible dimensions can instead be achieved only when the Drude weight is sufficiently low, as both increasing W and decreasing D shift the plasmonic resonances to lower frequencies (Fig. 2e, left). Even in this case, however, care must be taken to confirm that the observed spectrum reflects a true Drude response rather than a Phantom-Drude one (see SI).

One key aspect for the appearance of the Phantom-Drude response in design (a) is the momentum-dependent amplitude decay of the plasmonic self-cavity modes: lower-frequency modes exhibit higher amplitudes, while higher-frequency modes decay in amplitude, as illustrated with the blue dashed arrow in the left panel of Fig. 2d. This behavior originates from the unscreened plasmons in the transmission line gap, whose restoring force is proportional to q , yielding momentum-dependent resonance amplitudes. In contrast, screened plasmons have a momentum-independent restoring force and therefore exhibit equal resonance amplitudes at all excited momenta. As the hybrid screened/unscreened self-cavity modes shift to lower frequencies with increasing sample width or decreasing Drude weight, their superposition can mimic a Drude spectrum, where conductivity decreases with frequency.

In contrast, the 2D material in design (b) is predominantly screened due to the narrow transmission line gap ($W_2 \ll W_1$). As a result, the self-cavity modes exhibit the characteristics of screened 2D plasmons with uniform amplitudes across all excited momenta (see dashed blue arrow in center panel of Fig. 2d). Consequently, the resulting superposition of plasmonic modes does not mimic a Drude response, even as the sample width W is increased or the Drude weight D is decreased (see Fig. 2d,e, center panels). We note that the model does not account for Landau damping of high-momentum modes or other momentum-dependent scattering mechanisms, which could suppress or broaden higher-momentum excitations.

While we focus here on two representative cases, design (a) with $W_1 = W_2$ and $W_0 = 0$, and design (b) where

$W_2 \ll W_1$ and $W_0 = 0$, we have also simulated a wide range of geometries with $W_2 \neq W_1$ and $W_0 \neq 0$ (see SI). These simulations reveal that the Phantom-Drude response persists in all cases, disappearing only in the limit $W_2 \ll W_1$ and $W_0 = 0$, corresponding to design (b).

Finally, when a 2D material is placed in direct ohmic contact with the transmission line, as shown in design (c) of Fig. 2c, a true Drude response ($F = 0$ at all frequencies) is observed regardless of the sample width or Drude weight (see Fig. 2d,e, right panels). In the 2D material, the THz-driven current primarily flows in and out of the metal traces to which the sample is ohmically contacted. Unlike in other designs, this prevents charge accumulation at the edges, and no restoring force arises to form plasmonic standing waves. This principle is illustrated in Figures 2a,b,c.

Based on these three design characterizations, the potential for a Phantom-Drude response arises only in a transmission line geometry where $W_2 \ll W_1$ and $W_0 \ll W_1$, so that the plasmons that form in the unscreened regions generate self-cavity resonances with momentum-dependent amplitudes. This also requires that the 2D material is electrically isolated from the transmission line by an insulating layer such as hBN (design (a)). While design (b) can also produce a broad spectrum, this design has a clear cavity response and is therefore less prone to misinterpretation. Design (c), where the 2D material is in direct ohmic contact with the transmission line, offers the most reliable conditions for observing a true Drude response regardless of device size or conductivity, assuming a perfect ohmic contact can be made to the sample.

Having established how sample size and Drude weight govern the appearance of a Phantom-Drude response in design (a), we now examine the role of linewidth. In principle, self-cavity modes with infinitely narrow linewidths would produce clearly distinguishable resonances, eliminating confusion with a Drude response (see SI). However, as the linewidth increases, whether due to enhanced intrinsic electron scattering or inhomogeneous broadening, the ability to resolve individual modes diminishes, making a broad spectrum increasingly difficult to interpret. In the following, we examine two key mechanisms responsible for inhomogeneous linewidth broadening in on-chip THz spectroscopy.

Mechanism 2: Inhomogeneous linewidth broadening through irregularly shaped 2D materials.

Since plasmonic oscillations of the current density extend from one sample edge to the other, the resonance frequencies of the self-cavity modes are determined not only by the transmission line geometry but also by the overall sample width (the length is largely irrelevant; see Ref.23). If the sample extends irregularly beyond the transmission line, with non-rectangular boundary conditions, different regions along the THz pulse propagation direction will support self-cavity modes with varying

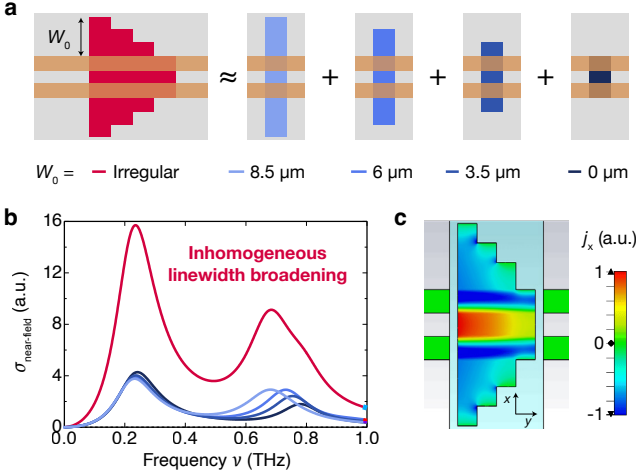


FIG. 3. Inhomogeneous linewidth broadening due to irregularly shaped 2D materials: **a** An irregularly shaped 2D material embedded in on-chip THz spectroscopy can be decomposed into slices of fixed width (here, $2.5\mu\text{m}$). Since the frequencies of the self-cavity modes strongly depend on the local width W_0 of the part of the 2D material extending the transmission line, the overall near-field optical conductivity spectrum of the irregular flake can be approximated as the sum of the responses from each individual slice. **b** Full 3D electromagnetic simulations are performed for both the entire irregular flake and its constituent slices. **c** Full 3D electromagnetic simulations of the current density distribution in the irregularly shaped sample at 0.686 THz and a phase of 103° . Distinct plasmonic modes of different wavelengths, and thus different resonance frequencies, form in different slices of the sample, whose combined response gives rise to the inhomogeneously broadened high-frequency peak shown in (b). Sample parameters: $W_1 = W_2 = 3\mu\text{m}$, $D = 24.5\text{ mS} \times \text{THz} \times \text{rad}$, $d_{\text{hBN}} = 25\text{ nm}$ and $\gamma = 1.5/(2\pi)\text{ THz}$.

wavelengths and resonance frequencies. As illustrated in Fig. 3, such a non-uniform 2D material can be conceptually divided into slices, each exhibiting a distinct plasmonic wavelength and thus resonance frequency. The superposition of these detuned modes leads to inhomogeneous broadening, and, if the overall resonance frequencies are sufficiently low, this can give rise to a Phantom-Drude response.

This issue can be mitigated by using precisely shaped, rectangular 2D materials, achievable through anodic oxidation lithography⁴³ or etching methods prior to assembling the vdW heterostructure.

Mechanism 3: Inhomogeneous linewidth broadening through hybridization with gate plasmons.

To fully explore the rich physics of vdW materials, electrostatic gates are essential for enabling *in situ* tuning of carrier density. However, incorporating such gates into on-chip THz spectroscopy introduces additional complexity. Since electrostatic gating requires the gate material to be at least weakly conductive to facilitate the formation of mirror charges and modulate

the carrier density, it unavoidably introduces THz absorption. To mitigate this effect, different groups have adopted a variety of strategies. Some have employed low-conductive gates, which exhibit a weak response in the THz regime^{26,28,44,45}. Others have implemented photo-gating techniques, in which a semiconducting transition-metal dichalcogenide (TMD) gate becomes conductive only under optical excitation²⁷. Alternatively, metallic graphite gates have been integrated into on-chip THz circuitry with a dedicated reference arm (Fig. 1a)^{23,39}, allowing direct characterization of the metallic gate response when the vdW material is at charge neutrality or in an insulating state.

A common strategy to mitigate gate contributions to the THz signal is to subtract them. However, as we demonstrate below, this approach can introduce complications. Plasmons can form in both vdW material and gate that hybridize strongly to form symmetric (in-phase) and antisymmetric (180 degrees out-of-phase) plasmonic modes (see Fig. 4a), that, depending on the conductivities and separations of the two layers, can significantly differ in resonance frequencies and spectral weight from their uncoupled counterparts (see Fig. 4b). In particular, when the gate has a low Drude weight ($D_{\text{gate}}/D_{\text{vdW material}} \ll 1$), an avoided crossing appears where the uncoupled gate and vdW material modes would otherwise cross in frequency. This avoided crossing signifies strong hybridization, highlighting that low-conductive gates can complicate the extraction of intrinsic vdW material properties. For example, a low-conductive gate's plasmonic resonance cannot be removed from a measured conductivity spectrum by simple subtraction, as such a procedure can even produce unphysical negative effective conductivities (see SI).

In contrast, when the layers are well separated by a thick hBN layer and/or the gate is much more conductive than the 2D material, the modes behave approximately as independent gate and 2D material plasmons (see Fig. 4b and also Ref.²³).

However, symmetric and antisymmetric modes only behave as uncoupled gate and 2D material plasmons if the gate-tunable heterostructure is placed in a homogeneously screened environment, such as in transmission line design (b) (see Fig. 2b). When the system follows transmission line design (a) (Fig. 2a), the situation becomes much more complex. Symmetric and antisymmetric modes can form both in the screened regions beneath the metal traces and also in the unscreened regions in the transmission line gap and outside the transmission line, with different dispersion relations (see SI). As the antisymmetric unscreened modes in the W_0 and W_2 regions (see Fig. 4a) have comparable resonance frequencies to the screened antisymmetric and symmetric modes in the W_1 regions, they can resonantly enhance the coupling of the screened modes, even of different momenta²³. In some cases, this can push the system into the *ultrastrong*

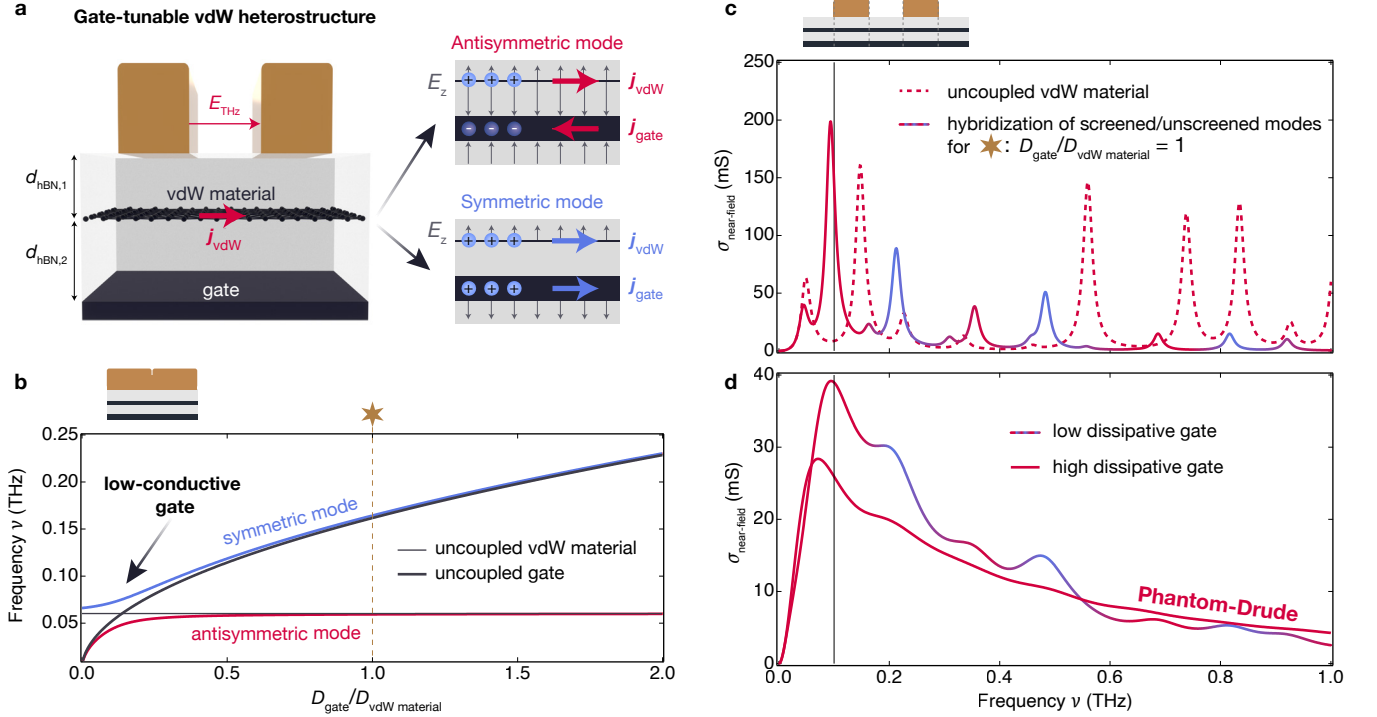


FIG. 4. **The challenge of low-conductive gates:** **a** In on-chip THz spectroscopy of gate-tunable vdW heterostructures, plasmonic modes in the vdW layer and nearby gate strongly couple due to their nanometer separation, forming hybrid symmetric (in-phase) and antisymmetric (out-of-phase) excitations. **b** Calculated resonance frequencies of hybrid and uncoupled modes versus gate-to-vdW material Drude weight ratio. Highly conductive gates yield weak hybridization, while low-conductive gates cause strong mode mixing and large frequency shifts. **c** Near-field conductivity spectra for gate-tunable vdW heterostructures in a transmission line of design (a) (see Fig. 2a). Two cases are compared: a perfectly screened vdW layer with a thick metallic gate (dashed red) and a vdW layer with a lower conductive gate where $D_{\text{gate}}/D_{\text{vdW material}} = 1$ (red-blue). In the latter, antisymmetric (vdW material-like, red) and symmetric (gate-like, blue) hybrid plasmon modes appear. The antisymmetric modes shift to lower frequencies due to coupling with the symmetric modes, a result of resonant interaction at the dielectric boundaries provided by the metal trace edges, as described in Ref.²³. **d** When the scattering rate is increased to $\gamma_{\text{gate}} = \gamma_{\text{vdW material}}$, distinct spectral features from multiple resonances remain visible (red-blue curve). However, if the gate's scattering rate becomes much larger than that of the vdW material, both the symmetric (blue) and antisymmetric (red) modes broaden significantly, merging into a smooth, featureless Phantom-Drude response (red curve). Sample parameters for panel (b): momentum $q = \pi/(39\mu\text{m})$, $D_{\text{vdW material}} = 43.35 \text{ mS} \times \text{THz} \times \text{rad}$ and $d_{\text{hBN},1} = 20 \text{ nm}$. Sample parameters for panels (c) and (d): $W_0 = W_1 = W_2 = 13 \mu\text{m}$, $d_{\text{hBN},1} = 20 \text{ nm}$, $d_{\text{hBN},2} = 100 \text{ nm}$, $D_{\text{vdW material}} = D_{\text{gate}} = 34.05 \text{ mS} \times \text{THz} \times \text{rad}$. Scattering rates in (c): $\gamma_{\text{gate}} = \gamma_{\text{vdW material}} = 0.02 \text{ THz}$. Scattering rates in (d): $\gamma_{\text{gate}} = \gamma_{\text{vdW material}} = 0.12 \text{ THz}$ (red-blue) and $\gamma_{\text{gate}} = 5 \times \gamma_{\text{vdW material}} = 0.60 \text{ THz}$ (red).

coupling regime^{46,47}, where the hybrid mode splitting exceeds 10% of the original resonance frequencies.

This type of coupling has a key consequence: in a homogeneously screened heterostructure, symmetric and antisymmetric plasmonic modes can closely resemble the uncoupled modes of the gate and the vdW material. As shown in Fig. 4b, when the gate and vdW material have comparable Drude weights ($D_{\text{gate}}/D_{\text{vdW material}} \approx 1$), the resonance frequency of the antisymmetric (vdW material-like) mode remains essentially unchanged, even as the gate conductivity increases beyond this ratio. In contrast, this behavior changes dramatically in a micropatterned dielectric environment, such as that introduced by transmission line design (a). As illustrated in Fig. 4c, the antisymmetric mode, originally resembling that of the uncoupled vdW material (dashed red), is

shifted to lower frequencies (solid red) due to hybridization with symmetric, gate-like modes (solid blue), even at $D_{\text{gate}}/D_{\text{vdW material}} = 1$.

Furthermore, hybridization with the gate affects not only the resonance frequencies but also the linewidths of the vdW material-like modes. When the gate exhibits high scattering rates, the increased damping broadens not only the symmetric gate-like mode but also the antisymmetric mode associated with the 2D material, leading to an artificially broadened spectral response of the vdW material. When many such broadened hybrid modes lie within the measurement bandwidth, their superposition can again lead to a Phantom-Drude response (Fig. 4d). Fitting such a broadened spectrum with a Drude model yields apparent parameters $\gamma_{\text{Phantom}} = 0.42 \text{ THz}$ and $D_{\text{Phantom}} = 63.44 \text{ mS} \times \text{THz} \times \text{rad}$ that deviate by over

400 % from the true intrinsic values of $\gamma = 0.1$ THz and $D = 43.35 \text{ mS} \times \text{THz} \times \text{rad}$ (see SI).

These findings highlight that, while low-conductive gates may initially seem like a straightforward choice for on-chip THz spectroscopy, they can complicate data interpretation by strongly modifying the response of a vdW material and potentially giving rise to a Phantom-Drude response. Such gates are most effective when intentionally used for cavity control protocols, provided they are carefully engineered in thickness and dimensions to limit the number of hybridizing self-cavity modes within the experimental sensitivity range²³.

In contrast, to probe the intrinsic response of a gate-tunable vdW material with minimal disturbance, a highly conductive gate, such as a 20 nm to 30 nm thick graphite flake, separated from the 2D material by a ~ 100 nm hBN spacer and embedded in a transmission line of design (b) provides an effective solution. In this “sensing cavity” configuration²³, coupling and linewidth broadening are strongly suppressed, and the gate contribution can be reliably subtracted using the on-chip THz architecture with built-in referencing (Fig. 1a)³⁹. Graphite flakes are widely employed in high-quality DC transport experiments for their reliability and low disorder (Fig. S11 of Ref.¹⁰) and allow symmetric, precise carrier density control for both electron and hole doping down to millikelvin temperatures. This is advantageous, as it indicates that the most effective approach for on-chip THz spectroscopy is to use standard graphite gates for vdW heterostructures, while carefully considering boundary conditions and flake thicknesses.

Discussion and outlook. By demonstrating that Phantom-Drude responses can emerge in on-chip THz spectra due to choices in sample size, transmission line geometry, vdW material, gate shapes, and gate material, this article highlights an important response regime. We provide design guidelines to enable selective probing of either Drude behavior or cavity electrodynamics in gate-tunable vdW heterostructures, both of which are well suited for extracting intrinsic material parameters. Although this article focused on responses of metallic 2D materials, the same principles extend to systems supporting other collective modes such as phonons, excitons, or plasmons in strange metals and superconductors³².

Looking ahead, the analytical framework developed for 2D materials in on-chip THz spectroscopy³² opens new avenues for tailoring sample designs to probe intricate spectral signatures of emergent phenomena in 2D quantum materials. Importantly, while our discussion centers on a specific on-chip THz spectroscopy circuit featuring two parallel metal traces, the underlying design principles for vdW heterostructures are broadly applicable. They can be readily adapted to other on-chip THz circuit architectures and may provide valuable guidance for a wide range of near-field techniques.

Funding

M.H.M., H.M.B. and M.W.D. acknowledge support from the Alexander von Humboldt Foundation. H.M.B. acknowledges financial support from the European Union under the Marie Skłodowska-Curie Grant Agreement no. 101062921 (Twist-TOC). G.K. acknowledges support by the German Research Foundation through the Cluster of Excellence CUI: Advanced Imaging of Matter (EXC 2056, project ID 390715994). We acknowledge support by the Deutsche Forschungsgemeinschaft (DFG, German Research Foundation) - 508440990 and 531215165 (Research Unit ‘OPTIMAL’). We acknowledge support from the Max Planck-New York Center for Non-Equilibrium Quantum Phenomena. This research was developed with funding from the Defense Advanced Research Projects Agency (DARPA) under the QUAMELEON Advanced Research Concept. The views, opinions and/or findings expressed are those of the authors and should not be interpreted as representing the official views or policies of the Department of Defense or the U.S. Government.

Acknowledgements

We acknowledge fruitful discussions with Dante Kennes.

Competing interests

The authors declare no competing interests.

Data, materials and code availability

Data available upon request.

Author contributions

G.K. and J.W.M. conceived the idea of the project. G.K. performed the analytical theory calculations using the theory developed by M.H.M. with support of G.K., A.M.P. and T.M.. T.M. performed the full 3D electromagnetic simulations with the aid of G.M.. H.M.B, M.H.M., M.W.D and A.M.P participated in the evolution of the ideas and impact within the field. G.K. visualized the data with support from M.W.D.. G.K. wrote the initial manuscript with support in reviewing and editing by all authors. J.W.M. supervised the overall project with support in mentoring from H.M.B..

-
- * Corresponding author: gunda.kipp@mpsd.mpg.de
† Corresponding author: jm5382@columbia.edu
- [1] Cao, Y. *et al.* Unconventional superconductivity in magic-angle graphene superlattices. *Nature* **556**, 43–50 (2018). URL <https://doi.org/10.1038/nature26160>.
 - [2] Mak, K. F. & Shan, J. Semiconductor moiré materials. *Nature Nanotechnology* **17**, 686–695 (2022). URL <https://doi.org/10.1038/s41565-022-01165-6>.
 - [3] Calderón, M. J. & Bascones, E. Correlated states in magic angle twisted bilayer graphene under the optical conductivity scrutiny. *npj Quantum Materials* **5**, 57 (2020). URL <https://doi.org/10.1038/s41535-020-00258-6>.
 - [4] Cao, Y. *et al.* Strange metal in magic-angle graphene with near planckian dissipation. *Phys. Rev. Lett.* **124**, 076801 (2020). URL <https://link.aps.org/doi/10.1103/PhysRevLett.124.076801>.
 - [5] Jindal, A. *et al.* Coupled ferroelectricity and superconductivity in bilayer td-moTe_2 . *Nature* **613**, 48–52 (2023). URL <https://doi.org/10.1038/s41586-022-05521-3>.
 - [6] Xia, Y. *et al.* Superconductivity in twisted bilayer wSe_2 . *Nature* **637**, 833–838 (2025). URL <https://doi.org/10.1038/s41586-024-08116-2>.
 - [7] Basov, D. N., Asenjo-Garcia, A., Schuck, P. J., Zhu, X. & Rubio, A. Polariton panorama. *Nanophotonics* **10**, 549–577 (2020).
 - [8] Xie, Y. *et al.* Spectroscopic signatures of many-body correlations in magic-angle twisted bilayer graphene. *Nature* **572**, 101–105 (2019). URL <https://doi.org/10.1038/s41586-019-1422-x>.
 - [9] Armitage, N. Electrodynamics of correlated electron systems. *arXiv preprint arXiv:0908.1126* (2009).
 - [10] Zibrov, A. A. *et al.* Tunable interacting composite fermion phases in a half-filled bilayer-graphene landau level. *Nature* **549**, 360–364 (2017). URL <https://doi.org/10.1038/nature23893>.
 - [11] Nuckolls, K. P. & Yazdani, A. A microscopic perspective on moiré materials. *Nature Reviews Materials* **9**, 460–480 (2024). URL <https://doi.org/10.1038/s41578-024-00682-1>.
 - [12] Park, H. *et al.* Observation of fractionally quantized anomalous hall effect. *Nature* **622**, 74–79 (2023). URL <https://doi.org/10.1038/s41586-023-06536-0>.
 - [13] Balents, L., Dean, C. R., Efetov, D. K. & Young, A. F. Superconductivity and strong correlations in moiré flat bands. *Nature Physics* **16**, 725–733 (2020). URL <https://doi.org/10.1038/s41567-020-0906-9>.
 - [14] Hillenbrand, R., Abate, Y., Liu, M., Chen, X. & Basov, D. N. Visible-to-thz near-field nanoscopy. *Nature Reviews Materials* **10**, 285–310 (2025). URL <https://doi.org/10.1038/s41578-024-00761-3>.
 - [15] Hillenbrand, R., Abate, Y., Liu, M., Chen, X. & Basov, D. N. Visible-to-thz near-field nanoscopy. *Nature Reviews Materials* **10**, 285–310 (2025). URL <https://doi.org/10.1038/s41578-024-00761-3>.
 - [16] Chen, J. *et al.* Optical nano-imaging of gate-tunable graphene plasmons. *Nature* **487**, 77–81 (2012). URL <https://doi.org/10.1038/nature11254>.
 - [17] Cocker, T. L. *et al.* An ultrafast terahertz scanning tunnelling microscope. *Nature Photonics* **7**, 620–625 (2013). URL <https://doi.org/10.1038/nphoton.2013.151>.
 - [18] von Hoegen, A. *et al.* Visualizing a terahertz superfluid plasmon in a two-dimensional superconductor (2025). URL <https://arxiv.org/abs/2506.08204>. 2506.08204.
 - [19] Seifert, T. *et al.* Efficient metallic spintronic emitters of ultrabroadband terahertz radiation. *Nature Photonics* **10**, 483–488 (2016). URL <https://doi.org/10.1038/nphoton.2016.91>.
 - [20] Handa, T. *et al.* Terahertz emission from giant optical rectification in a van der waals material. *Nature Materials* (2025). URL <https://doi.org/10.1038/s41563-025-02201-1>.
 - [21] Helmrich, F. *et al.* Cavity-driven attractive interactions in quantum materials (2025). URL <https://arxiv.org/abs/2408.00189>. 2408.00189.
 - [22] Hillenbrand, R., Abate, Y., Liu, M., Chen, X. & Basov, D. N. Visible-to-thz near-field nanoscopy. *Nature Reviews Materials* **10**, 285–310 (2025). URL <https://doi.org/10.1038/s41578-024-00761-3>.
 - [23] Kipp, G. *et al.* Cavity electrodynamics of van der waals heterostructures. *Nature Physics* (2025). URL <https://doi.org/10.1038/s41567-025-03064-8>.
 - [24] Zhao, W. *et al.* Observation of hydrodynamic plasmons and energy waves in graphene. *Nature* **614**, 688–693 (2023).
 - [25] Potts, A. M. *et al.* Finite momentum cooper plasmons below the light cone in a superconducting thz micro-cavity. *in preparation* (2025).
 - [26] Gallagher, P. *et al.* Quantum-critical conductivity of the Dirac fluid in graphene. *Science* **364**, 158–162 (2019).
 - [27] Seo, J. *et al.* On-Chip Terahertz Spectroscopy for Dual-Gated van der Waals Heterostructures at Cryogenic Temperatures. *Nano Letters* **24**, 15060–15067 (2024).
 - [28] Chen, S.-D. *et al.* Direct measurement of terahertz conductivity in a gated monolayer semiconductor. *ACS nano* (2025).
 - [29] Potts, A. M. *et al.* On-chip time-domain terahertz spectroscopy of superconducting films below the diffraction limit. *Nano Letters* **23**, 3835–3841 (2023).
 - [30] Island, J. O. *et al.* On-chip terahertz modulation and emission with integrated graphene junctions. *Applied Physics Letters* **116** (2020).
 - [31] Sterbentz, R. M. & Island, J. I. *On-Chip Sub-Diffraction THz Spectroscopy of Materials and Liquids* (IntechOpen, 2023).
 - [32] Michael, M. H. *et al.* Resolving self-cavity effects in two-dimensional quantum materials (2025). URL <https://arxiv.org/abs/2505.12799>. 2505.12799.
 - [33] McIver, J. W. *et al.* Light-induced anomalous hall effect in graphene. *Nature physics* **16**, 38–41 (2020).
 - [34] Zhong, Z., Gabor, N. M., Sharping, J. E., Gaeta, A. L. & McEuen, P. L. Terahertz time-domain measurement of ballistic electron resonance in a single-walled carbon nanotube. *Nature nanotechnology* **3**, 201–205 (2008).
 - [35] Wang, E. *et al.* Superconducting nonlinear transport in optically driven high-temperature k_3C_{60} . *Nature Communications* **14**, 7233 (2023).
 - [36] Adelinia, J. D. *et al.* Probing optically driven k_3C_{60} thin films with an ultrafast voltmeter. *Structural Dynamics* **12**, 024503 (2025). URL <https://doi.org/10.1063/4.0000295>.
 - [37] Karnetzky, C. *et al.* Towards femtosecond on-chip electronics based on plasmonic hot electron nano-emitters. *Nature communications* **9**, 2471 (2018).

- [38] Yoshioka, K. *et al.* On-chip transfer of ultrashort graphene plasmon wave packets using terahertz electronics. *Nature Electronics* **7**, 537–544 (2024).
- [39] Kussyak, K. *et al.* Monolithic optoelectronic circuit design for on-chip terahertz applications. *accepted in APL photonics* (2025).
- [40] Chen, S.-D. *et al.* Terahertz electrodynamics in a zero-field wigner crystal (2025). URL <https://arxiv.org/abs/2509.10624>. 2509.10624.
- [41] Marulanda, E., Costa, F. L., Kawahala, N. M. & Hernandez, F. G. G. Windowing in terahertz time-domain spectroscopy: resolving resonances in thin-film samples (2025). URL <https://arxiv.org/abs/2507.00729>. 2507.00729.
- [42] Horng, J. *et al.* Drude conductivity of Dirac fermions in graphene. *Physical Review B—Condensed Matter and Materials Physics* **83**, 165113 (2011).
- [43] Li, H. *et al.* Electrode-free anodic oxidation nanolithography of low-dimensional materials. *Nano Letters* **18**, 8011–8015 (2018). URL [10.1021/acs.nanolett.8b04166](https://doi.org/10.1021/acs.nanolett.8b04166).
- [44] Hesp, N. C. *et al.* Wse2 as transparent top gate for infrared near-field microscopy. *Nano Letters* **22**, 6200–6206 (2022).
- [45] Sterbentz, R. M. *et al.* Gating monolayer and bilayer graphene with a two-dimensional semiconductor. *npj 2D Materials and Applications* **9**, 29 (2025).
- [46] Forn-Díaz, P., Lamata, L., Rico, E., Kono, J. & Solano, E. Ultrastrong coupling regimes of light-matter interaction. *Reviews of Modern Physics* **91**, 025005 (2019).
- [47] Frisk Kockum, A., Miranowicz, A., De Liberato, S., Savasta, S. & Nori, F. Ultrastrong coupling between light and matter. *Nature Reviews Physics* **1**, 19–40 (2019).